A Combined Opening-Sliding Formulation for use in Modeling Geomaterial Deformation and Fracture Patterns

D. A. Weed , C. D. Foster * and M. H. Motamedi

Department of Civil and Materials Engineering, University of Illinois at Chicago, Chicago, IL, USA,
e-mail: fosterc@uic.edu

Abstract: Within a finite element context, the embedded strong discontinuity approach for strain localization has been used extensively to model localized deformation and fracture in geomaterials. As a fracture propagates, any changes in orientation will inhibit sliding and force the surfaces, in some locations, to open. Some previous models feature only a single sliding degree of freedom. As the surfaces slip in such models, an artificial hardening occurs, creating a geometric locking effect. To this end, we implement a formulation, which, in addition to sliding, possesses an opening degree of freedom. We develop a constitutive model that allows for coupled opening and shearing displacement in tension, as well as pure sliding in compression. This paper compares the single degree of freedom formulation with the model containing both degrees of freedom. We show that the locking effect is alleviated. In addition, a method for increasing the robustness of softening problems is featured.

Keywords and phrases: strong discontinuity, enhanced strain finite element, bifurcation, localized deformation, simulation robustness.

1. Introduction

The numerical modeling of geomaterials, especially in the context of finite element analysis, has a wide and varied base of research behind it. As part of these developments over the past two decades, embedded discontinuities

---

*Corresponding Author. Tel.: +1-312-996-8086, Fax:+1-312-996-2426.

have been investigated for use in numerical models which seek to capture failure due to localized softening. The concept of a so-called weak discontinuity was developed in order to capture narrow shear bands of deformation within materials [3, 38]. Shear bands were first described in metals by Tresca [39]. Later, this nomenclature was adopted by the geomechanics community in order to describe similar phenomenon seen in soil and rock-like materials. Subsequently, numerical models were developed in order to replicate this behavior in simulations. Precipitated from this line of research was the strong discontinuity approximation. When the width of the discontinuity is small compared to that of the overall structure the weak discontinuity may be simplified by reducing it to zero width. Simo and co-workers showed in seminal reports [36, 37] that the post-localization softening modulus of the material as well as the plastic multiplier necessarily take on a distributional representation. In addition to this representation, they introduced a re-parametrized displacement and strain field which is suited for capturing both measures of deformation within a finite element context.

The model presented in this paper is an extension of the Mohr-Coulomb slip model for geological materials in [5, 10, 13, 31, 32]. The main contribution of this paper is the introduction of a post-localization constitutive model allowing for slip in directions both tangential and normal to a given discontinuity band. The impetus for this is two-fold. In reality, as geomaterials begin to localize and subsequently fail in either the compressive or tensile regime, material may not only slide but also, noticeable movement in the direction normal to the failure surface is observed. Even for far-field compression, the development of a model which takes into account the interaction of both compressive and tensile traction necessary.

Carol et al. [8] developed a hyperbolic yield surface in order to capture the effect of tension and a linear one for the purely compressive regime. This model was later adopted by Galvez, et al. [15] for the purposes of simulating material failure in masonry structures. The model in this paper is similar to that of Carol and Galvez in that it captures the aforementioned deformation regimes. Camacho and Ortiz [7] developed a model which features an elliptical interaction between the shear and normal tractions on a given deformation band. In this model, a material parameter is employed to control the contribution of the shear traction on the surface, a feature which is later used in [40]. In a similar a vein, we develop a model which features elliptical interactions between both the tractions and displacements (normal

and tangential to the surface cf. [41]), based on the material's strain energy release rate.

Secondly, in [13] simulations yielded results which revealed that a model only incorporating a single, sliding degree of freedom gave rise to geometric locking which was mesh-dependent. Specifically, this effect arose due to the model's inability to accurately capture opening displacements. From this observation, the conjecture was that remedies such as extra degrees of freedom [23, 26] would alleviate geometric locking. The authors in this paper took the latter approach by developing a constitutive model which features both opening and sliding degrees of freedom on the discontinuity surface. When the band is in compression, it is only subject to deformation tangential to its surface. Hence, friction and cohesion forces impede sliding on the localization band. However, when tension is present the band experiences a combination of opening normal to the surface in addition to the aforementioned tangential sliding, albeit without friction. We show that such a model presents a more realistic depiction of the mechanics of softening behavior within soil-based materials. Through several benchmark examples, this paper shows that the currently proposed constitutive model alleviates the spurious geometric locking effect seen in [13].

In this particular study, we focus on a damage-like formulation which assumes elastic unloading toward the origin and the tradition of cohesive zone formulations. For simplicity, we will consider a constant friction coefficient. However, this is not a requirement. By ramping up the friction coefficient as the cohesion degrades, we can recreate the simplified slip weakening formulation as described in Borja and Foster [5]. Variable friction as detailed in [12] and [13] can also be implemented.

Softening problems within the strong discontinuity framework are well known to have robustness and stability issues [4, 20, 27]. To this end, we incorporate a combined implicit-explicit integration method (Impl-Ex), modified from a scheme devised by Oliver and co-workers [28], which renders the local stiffness matrices associated with softened elements positive definite. We show that this allows problems with complex geometries to converge, whereas using a fully implicit integration scheme does not.

The remainder of the paper is structured as follows: Section 2 gives a general overview of strong discontinuity kinematics in the context of small strain. Additionally, in this section, the localization criterion, which indicates the

onset of the formation of a strong discontinuity, is given a brief review. Section 3 briefly discusses some fundamental aspects of an enhanced strain finite element. The constitutive model for slip weakening within a localized element is described in Section 4. The numerical implementation of the model is given in Section 5. Section 6 shows the derivation of the stiffness formulation. Numerical examples and closing remarks conclude the paper.

A summary of the symbolic notation used throughout this paper is noted here. Boldface quantities denote vectors and tensors, e.g., $(\boldsymbol{a})_{ij} = a_{ij}$. The symmetric dyadic product in index notation is $(\boldsymbol{a} \otimes \boldsymbol{b})_{ij}^s = \frac{1}{2}(a_i b_j + a_j b_i)$, where the superscript "s" denotes a symmetric second-order tensor. The dot product is expressed as $\boldsymbol{a} \cdot \boldsymbol{b} = a_i b_i$, where Einstein's summation convention is used. The inner product symbol ":" is used for contraction of two second-order tensors as $\boldsymbol{a} : \boldsymbol{b} = a_{ij} b_{ij}$ or for the contraction of a fourth-order tensor and a second order tensor as $\boldsymbol{c} : \boldsymbol{a} = c_{ijkl} a_{kl}$. The symmetric gradient operator acting on a vector is written as $(\boldsymbol{\nabla}^s \boldsymbol{a})_{ij} = \frac{1}{2}(a_{i,j} + a_{j,i})$.

2. Kinematics

2.1. Continuum Equations

Here we describe the kinematical relationship between continuous and discontinuous displacements within an arbitrary continuous volume (Figure 1). Note that for the purposes of this study, our analysis is relegated to the realm of infinitesimal strains. The continuous displacements are distributed throughout the volume while the discontinuous displacements are contained on the discontinuity surface S. The total displacement field in the body is given by the form:

$$\boldsymbol{u} := \bar{\boldsymbol{u}} + [\![\boldsymbol{u}]\!] H_S(\boldsymbol{x}) \tag{2.1}$$

where $\bar{\boldsymbol{u}}$ is the vector of continuous displacements and $[\![\boldsymbol{u}]\!]$ designates the vector of displacements along the strong discontinuity. This vector takes the form:

$$[\![\boldsymbol{u}]\!] = \boldsymbol{\zeta} = \zeta_s \boldsymbol{l} + \zeta_n \boldsymbol{n} \tag{2.2}$$
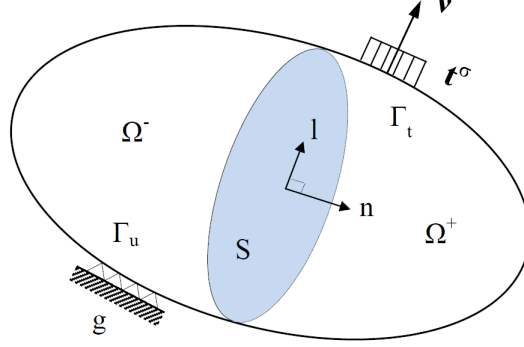
Fig 1: Arbitrary volume with embedded strong discontinuity surface

Where $\boldsymbol{l}$ and $\boldsymbol{n}$ are unit vectors which are tangential and normal to the discontinuity surface, respectively.

$H_S(\boldsymbol{x})$ is the Heaviside function across the discontinuity surface S defined by the conditions

$$H_S(\boldsymbol{x}) = \left\{ \begin{array}{lll} 1 & \text{if} & \boldsymbol{x} \in \Omega^+ \\ 0 & \text{if} & \boldsymbol{x} \in \Omega^- \end{array} \right. \tag{2.3}$$

The strain tensor is found by taking the symmetric part of the gradient of the displacement vector:

$$\boldsymbol{\epsilon} := \nabla^s \boldsymbol{u} = \nabla^s \bar{\boldsymbol{u}} + \nabla^s [\![\boldsymbol{u}]\!] H_S + ([\![\boldsymbol{u}]\!] \otimes \boldsymbol{n})^s \delta_S \tag{2.4}$$

where $\nabla H_S = \boldsymbol{n}\delta_S$. The physical meaning of the last term is that the strain is unbounded on the discontinuity surface S.

For the purposes of this study, the jump magnitude is considered to be spatially invariant (piece-wise constant across the elements). Thus the second term is omitted from the equation, leaving the final form of

$$\boldsymbol{\epsilon} := \nabla^s \boldsymbol{u} = \nabla^s \bar{\boldsymbol{u}} + ([\![\boldsymbol{u}]\!] \otimes \boldsymbol{n})^s \delta_S \tag{2.5}$$

2.2. Localization Condition

In this section, the procedure that is used to detect the onset of strain localization is outlined. Hill [17] investigated the physics of wave propagation in solids in order to determine the onset of inelastic behavior therein. Rudnicki and Rice, in [35], built off of this work introducing a mathematical framework for detecting shear band localization. This formulation has since been extended to the case of displacement discontinuities as well as strain discontinuities ([6, 30] among others). Since then, bifurcation theory has been widely used to determine the onset of softening behavior of various geomaterials.

To begin, we posit that at any given time, the traction rate along the discontinuity surface must be continuous. Using a general non-associative plasticity model, i.e., where F is an arbitrary yield function and G is a plastic potential, the traction rate is written as

$$\dot{\boldsymbol{t}} = \dot{\boldsymbol{\sigma}} \cdot \boldsymbol{n} = \boldsymbol{n} \cdot \boldsymbol{c}^e : \left(\dot{\boldsymbol{\epsilon}} - \dot{\lambda} \frac{\partial G}{\partial \boldsymbol{\sigma}} \right) \tag{2.6}$$

Where $\boldsymbol{c}^e$ is the elastic modulus tensor and $\dot{\lambda}$ is the rate of the plastic multiplier.

For a discontinuity in the displacement field, the plastic multiplier must have a distributional form. From [6] $\dot{\lambda} = \dot{\lambda}_\delta \delta_S$

where $\dot{\lambda}_\delta = \frac{1}{\chi} \frac{\partial G}{\partial \boldsymbol{\sigma}} : \boldsymbol{c}^e : (\llbracket \dot{\boldsymbol{u}} \rrbracket \otimes \boldsymbol{n})^S$ and $\chi = \frac{\partial F}{\partial \boldsymbol{\sigma}} : \boldsymbol{c}^e : \frac{\partial G}{\partial \boldsymbol{\sigma}}$

Substituting this into (2.7) yields

$$\dot{\boldsymbol{t}} = \underbrace{\boldsymbol{n} \cdot \boldsymbol{c}^e : \nabla^S \dot{\bar{\boldsymbol{u}}}}_{\dot{\bar{\boldsymbol{t}}}} + \underbrace{\boldsymbol{c}^{ep} : (\llbracket \dot{\boldsymbol{u}} \rrbracket \otimes \boldsymbol{n})^S}_{\dot{\boldsymbol{t}}_\delta} \delta_S \tag{2.7}$$

where the term $\boldsymbol{c}^{ep} = \boldsymbol{c}^e - \frac{1}{\chi} \boldsymbol{c}^e : \frac{\partial G}{\partial \boldsymbol{\sigma}} \otimes \frac{\partial F}{\partial \boldsymbol{\sigma}} : \boldsymbol{c}^e$ is the elastic-perfectly plastic tangent modulus.

In order for the traction to be bounded, the discontinuous part must vanish, hence

$$\dot{\boldsymbol{t}}_\delta = \boldsymbol{n} \cdot \boldsymbol{c}^{ep} : (\llbracket \dot{\boldsymbol{u}} \rrbracket \otimes \boldsymbol{n})^s = \boldsymbol{0}$$

Noting that $\llbracket \dot{\boldsymbol{u}} \rrbracket = \dot{\zeta} \boldsymbol{m}$, this expression can be re-written as

$$(\boldsymbol{n} \cdot \boldsymbol{c}^{ep} \cdot \boldsymbol{n}) \cdot \boldsymbol{m} = \boldsymbol{A} \cdot \boldsymbol{m} = \boldsymbol{0} \tag{2.8}$$

where $\boldsymbol{A}$ is known as the elastic-perfectly plastic acoustic tensor.

This quantity is zero only when $\boldsymbol{A}$ becomes singular, that is, when $\det(\boldsymbol{A}) = 0$.

Eq. 2.8 can be solved iteratively, as detailed in [29] and [42], in order to determine the direction of the jump, $\boldsymbol{m}$, along the discontinuity.

3. Post-localization Constitutive Model

3.1. *Yield Criteria*

Once localization has been detected and the orientation of the critical surface determined, the mechanics of the softening behavior on the surface must be defined. There are several ways to approach this model. Oliver [25] has shown that the continuum model can be used to induce a localized model. The great advantages of this approach are that a smooth and consistent transition from continuum to localized response is assured, and the material response is consistent with experimental data. However, it may also be argued that the mechanics of the localized material differ from the bulk continuum response since this is a separate mechanism. In this case, a separate constitutive model must be introduced for the localized behavior. The form of that model is the subject of this section.

The initial cohesion on the surface is determined to be consistent with the stress state at localization. The yield strength in pure tension may be different, and thus is assumed to differ by a constant factor of α_σ. The constant,

α_σ can be thought of as the reciprocal of the parameter β, which is described as a shear stress factor in Camacho and Ortiz [7]. Similarly, Alfaiate et al. [1] use a parameter which controls the contribution of the shear jump on the deformation band.

The yield function that we incorporate takes two forms. When compressive normal traction is present on the band, the yield function takes the form of a Mohr-Coulomb law (Eq. 3.1). In the case of tensile normal traction, the interaction between the shear and normal traction is assumed to be elliptical (Eq. 3.2).

$$\Phi_{\text{compression}} = 0 = |\tau - c \cdot \text{sign}(\zeta_s)| - f \tag{3.1}$$

$$\Phi_{\text{tension}} = 0 = \sqrt{(\tau)^2 + (\alpha_\sigma \langle\sigma\rangle)^2} - c \tag{3.2}$$

where $\sigma = \boldsymbol{n} \cdot \boldsymbol{\sigma} \cdot \boldsymbol{n}$ is the normal traction, $\tau = \boldsymbol{l} \cdot \boldsymbol{\sigma} \cdot \boldsymbol{n}$ the shear traction on the deformation band. ζ_s is the amount of slip in the direction parallel to the deformation band and c is the cohesion. $\langle\cdot\rangle$ are the Macaulay brackets $[\langle x\rangle = (x + |x|)/2]$, signifying the positive part of the quantity. Hence in compression, the normal traction only influences the yield function in the frictional traction $f = \mu \langle-\sigma\rangle$. For this study, we use a static coefficient of friction, though a variable coefficient, as in [5, 13], can be used.

3.2. *Cohesion Softening Formulation*

The cohesive formulation we will use takes the form of a traction-displacement relationship, common in the cohesive zone formulations such as [7, 11, 18]. This formulation follows the spirit of localized damage mechanics, so that the interface softens with increased displacement, but unloads elastically. Reloading is also elastic until the previous displacement level is reached, where damage continues (Figure 3). For our particular formulation, we use a linear form given by the equation

$$c = c_0 \left(1 - \frac{\zeta_{eq}}{\zeta^*}\right) \tag{3.3}$$

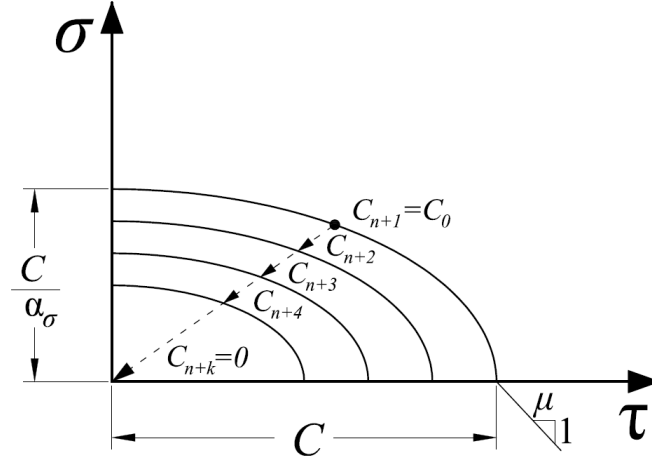Fig 2: Normal and shear traction interaction on yield surface

where c is exactly the cohesion along the surface in standard Mohr-Coulomb criteria, c_0 is the initial cohesion at the time of localization, ζ_{eq} is a weighted magnitude of the slip on the band and ζ^* is the slip distance until the cohesion completely degrades to zero.

In the literature, several other cohesion softening laws, particularly suited for brittle materials such as concrete, are bilinear [16, 44], exponential [9, 43], and power-law based [33]. For geomaterials however, a linear model for cohesion degradation seems to fit experimental data well [19, 34].

The initial cohesion is determined to be consistent with the bulk stress state at the moment of localization. In addition to linear softening we assume elastic unloading and reloading with respect to the equivalent traction and displacement.

We define a parameter $\zeta_c = \zeta^* (c_0 - c) / c_0$, which is the maximum equivalent slip magnitude observed on the slip surface up to the current time. The parameter k_s is defined as the slope of the unloading-reloading curve at a given value of ζ_c. Therefore, $k_s = c/\zeta_c$. On this portion of the curve, we also assume that the cohesion is frozen at a value of ζ_c, thus the explicit form of k_s is given by
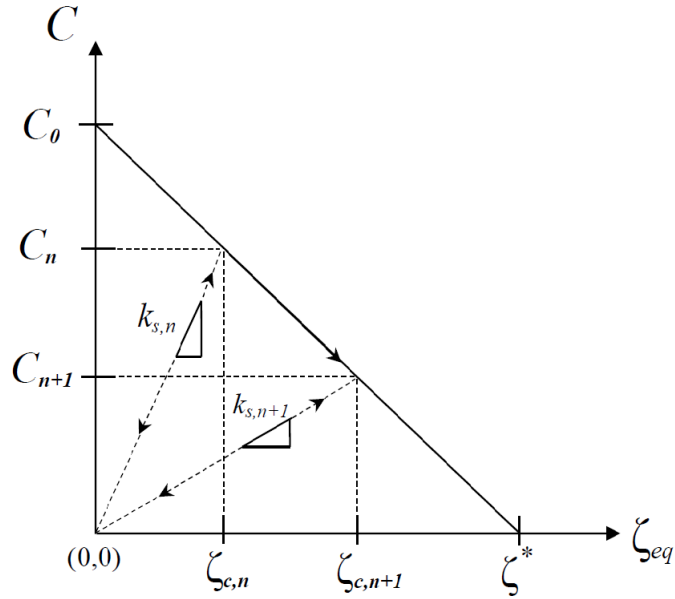
Fig 3: Cohesion softening law displaying different unloading-reloading curves at arbitrary time steps n and n+1

$$k_s = c_0 \left(1 - \frac{\zeta_c}{\zeta^*} \right) \frac{1}{\zeta_c}$$

$$= c_0 \left(\frac{1}{\zeta_c} - \frac{1}{\zeta^*} \right) \tag{3.4}$$

Further softening on the band can only occur when $\zeta_{eq} \geq \zeta_c$.

Remark: The assumption that the cohesion is constant on the unloading-reloading portion of the graph is a simplification but also one which is grounded in reality. One could imagine that, under very small displacement values, as the crack moves back and forth, some material will remain intact although it will stretch or elongate. It is quite possible for a cohesive material to undergo this process. For very small displacements, the material will deform but the overall cohesive force of the soil will remain intact.

3.3. *Tensile Regime*

In tension, the friction force is absent, therefore according to Eq. 3.2 the equivalent stress on the band is

$$\sigma_{eq} = c = \sqrt{\tau^2 + (\alpha_\sigma \sigma)^2} \tag{3.5}$$

We relate the stiffness parameter, k_s, to the traction on the band

$$
\begin{aligned}
\sqrt{\tau^2 + (\alpha_\sigma \sigma)^2} &= c \\
\vdots \quad &= c_0 \left(1 - \frac{\zeta_{eq}}{\zeta^*} \right) \\
\vdots \quad &= c_0 \left(1 - \frac{\zeta_{eq}}{\zeta^*} \right) \frac{\zeta_{eq}}{\zeta_{eq}} \\
\vdots \quad &= c_0 \left(\frac{1}{\zeta_{eq}} - \frac{1}{\zeta^*} \right) \zeta_{eq} \\
\sigma_{eq} \quad &= k_s \zeta_{eq}
\end{aligned}
\tag{3.6}
$$

where $\zeta_{eq} = \sqrt{\zeta_s^2 + (\alpha_\zeta \zeta_n)^2}$. The material parameter, α_ζ, signifies the differing weights of the opening and shear displacements.

We now postulate two balance laws which relate the tractions and displacements both normal and tangential to the deformation band:

$$
\begin{aligned}
\alpha_\sigma \sigma &= k_s \alpha_\zeta \zeta_n \tag{3.7} \\
\tau &= k_s \zeta_s. \tag{3.8}
\end{aligned}
$$

Eq. 3.7 can also be written as

$$
\begin{aligned}
\sigma &= \frac{\alpha_\zeta}{\alpha_\sigma} k_s \zeta_n \\
&= k_n \zeta_n
\end{aligned}
\tag{3.9}
$$

where k_n represents the stiffness in the direction of the normal traction on the band. If we rewrite this stiffness parameter, solving for α_σ, we have $\alpha_\sigma = \frac{\alpha_\zeta}{k_n}k_s$. This is substituted into Eq. 3.5 giving

$$\sigma_{eq} \;=\; \sqrt{\tau^2 + \left(\frac{\alpha_\zeta k_s}{k_n}\sigma\right)^2}.$$

Further, substituting the forms in the traction-displacement balance laws in Eqs. 3.7 and 3.8 yields

$$\sigma_{eq} = \sqrt{(k_s\zeta_s)^2 + (\alpha_\zeta k_s\zeta_n)^2}$$
$$= k_s\sqrt{\zeta_s^2 + (\alpha_\zeta\zeta_n)^2}$$
$$= k_s\zeta_{eq}$$

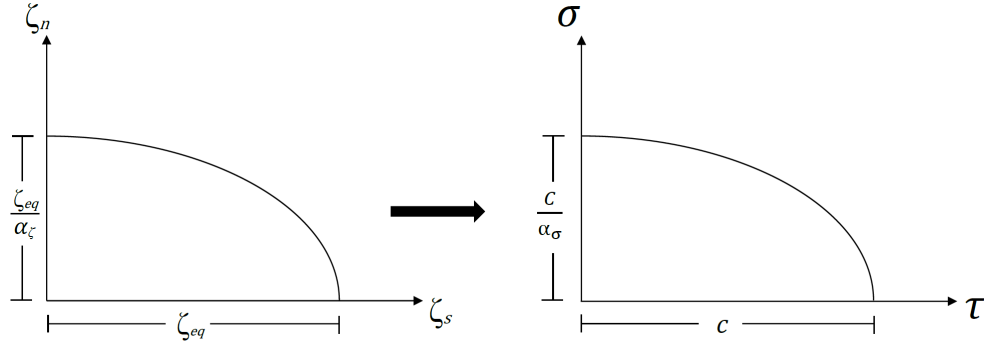which recovers Eq. 3.6, verifying the coupled nature of the tractions and displacements on the deformation band.

Fig 4: For a deformation band experiencing tension, the slip degrees of freedom are coupled with the tractions.

3.3.1. Determining the parameters α_σ and α_ζ

These parameters are related to one another vis à vis the fracture energy in each of the respective fracture modes. The specific fracture energy for Mode

I (opening) and Mode II (sliding) (Figure 5) is simply the area under the respective curves (cf. [45]). Therefore

$$G_I = \frac{1}{2}\frac{\zeta^*}{\alpha_\zeta}\frac{c}{\alpha_\sigma} \tag{3.10}$$
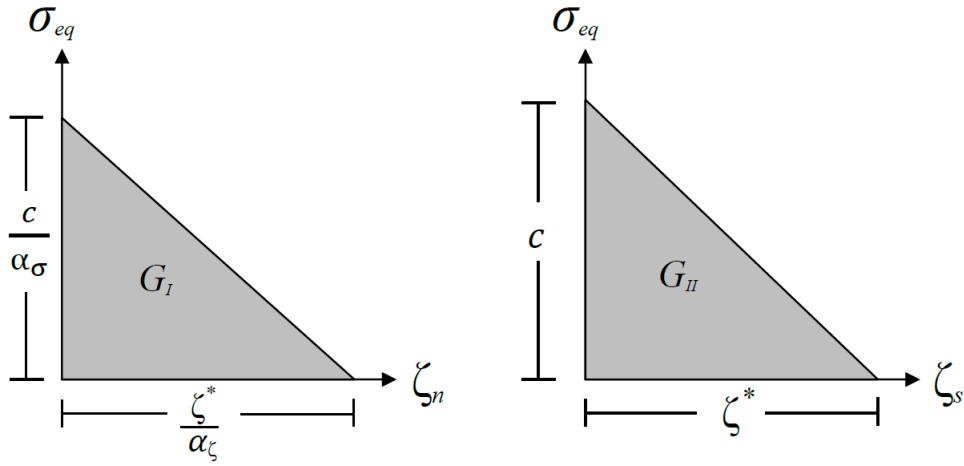
$$G_{II} = \frac{1}{2}\zeta^*c \tag{3.11}$$

Fig 5: The fracture energy for opening and sliding fractures

The fracture energy is related to the stress intensity factor, K, through the equation

$$G = \frac{K^2}{E}(1-\nu^2) \tag{3.12}$$

which is valid for plane strain.

Hence, the ratio of the corresponding stress intensity factors is

$$\left(\frac{K_{II}}{K_I}\right)^2 = \frac{G_{II}}{G_I} = \alpha_\zeta \cdot \alpha_\sigma \tag{3.13}$$

There are many solutions to Eq. 3.13, however in this study, we choose the solutions in which $\alpha_\zeta = \alpha_\sigma$. In [2], the empirical value for the ratio $\dfrac{K_{II}}{K_I}$ varies between 1.13, which corresponds to softer marble, and 2.19, for limestone. In this study, we simply choose $\alpha_\zeta = \alpha_\sigma \approx 2.0$. In a future study that will feature the combination of this model and the plasticity model detailed in [24], we choose a value closer to that of limestone (which is ≈ 2.14), for that will be the particular material of interest. It is worth noting that authors in [7] derived $\alpha_\zeta = 1/\alpha_\sigma$ on energy considerations. However, this creates equal fracture energy in Mode I and II, which is not observed in many materials.

3.4. Compressive Formulation

The cohesive formulation is exactly the same as in the tensile case. However, the normal effects on σ_{eq} are neglected. In other words, under compression $\sigma_{eq} = \tau$. In addition to this, the normal displacement on the band is assumed to be zero. Hence, $\tau = k_s \zeta_s$.

However, in addition to cohesive tractions, there is a friction force, defined earlier as $f = \mu \langle -\sigma \rangle$. Under compression, the frictional force acts independently of the displacement, and hence is always active. The final form of the traction balance in this case may be written as

$$|\tau - k_s \zeta_s| \leq f \tag{3.14}$$

where strictly less than implies no motion on the band, and equality allows for slip.

For many quasi-brittle materials, there is actually noticeable dilation along shear bands and fracture interfaces due to the mismatch of rough surfaces, wear, and the resulting gouge material [22]. However, this often small and is beyond the current scope of this work.

4. Finite Element Implementation

4.1. Re-parameterization of displacement field

Here, we use the parametrized form of the displacement introduced by Simo and co-workers [37]. Within a standard Assumed Enhanced Strain (AES) framework, the displacement field is recast such that the continuous part conforms to the standard finite element formulation and the discontinuous part is considered as an additional enhancement to the displacement field. Hence,

$$\boldsymbol{u}^h = \boldsymbol{u}^{h,conf} + \boldsymbol{u}^{h,enh} \tag{4.1a}$$

$$\boldsymbol{u}^h = \hat{\boldsymbol{u}}^h + [\![\boldsymbol{u}^h]\!] M_S^h(\boldsymbol{x}) \tag{4.1b}$$

where $M_S^h(\boldsymbol{x}) = H_S - f^h$. Hence,

$$\boldsymbol{u}^h = \left(\bar{\boldsymbol{u}}^h + [\![\boldsymbol{u}^h]\!] f^h\right) + [\![\boldsymbol{u}^h]\!] \left(H_S - f^h\right) \tag{4.1c}$$

The term, f^h, is an arbitrary smooth function which, on a given element with a discontinuity, meets the criteria

$$f^h = \begin{cases} 1 & \text{if} \quad e_n \in \Omega^+ \\ 0 & \text{if} \quad e_n \in \Omega^- \end{cases} \tag{4.2}$$

and e_n is the element node number. For this study, f^h takes the particular form of

$$f^h = \sum_{A=1}^{n_{en}} N_A H_S(\boldsymbol{x}_A) \tag{4.3}$$

where n_{en} is the set of active nodes within a given element, i.e. nodes that are in Ω^+. For each element, the conforming displacement field is composed of the continuous nodal displacements as well as the contribution of the displacements along the localization band. This part of the displacement "conforms" to the standard finite element shape functions, hence

$$\boldsymbol{u}^{h,conf} = \sum_{A=1}^{n_{en}} N_A \boldsymbol{d}_A \tag{4.4}$$

The strain tensor is obtained by taking the symmetric part of the gradient of the displacement in eq. (4.1c) yielding,

$$\boldsymbol{\epsilon}^h = \boldsymbol{B}\boldsymbol{d} + \left[\left(\boldsymbol{\zeta} \otimes \boldsymbol{n} \right)^s \delta_S - \left(\boldsymbol{\zeta} \otimes \nabla f^h \right)^s \right] \tag{4.5}$$

$$= \boldsymbol{\epsilon}^{h,conf} + \boldsymbol{\epsilon}^{h,enh}.$$

In terms of recovering the finite element stress, it is convenient to denote the strain in terms of a regular or continuous part and a singular or jump part:

$$\boldsymbol{\epsilon}^h = \underbrace{\boldsymbol{B}\boldsymbol{d} - \left(\boldsymbol{\zeta} \otimes \nabla f^h \right)^s}_{regular} + \underbrace{\left(\boldsymbol{\zeta} \otimes \boldsymbol{n} \right)^s \delta_S}_{singular} \tag{4.6}$$

as shown in [6], the finite element stress for localized elements is derived from the regular part of the strain, hence

$$\dot{\boldsymbol{\sigma}}^h = \boldsymbol{c}^e : \dot{\boldsymbol{\epsilon}}^{h,reg} \tag{4.7}$$

5. Numerical Implementation of Slip Model

The solution technique employed to solve the slip at the element level is a piecewise Newton-Raphson iteration. This particular approach is well-suited for the proposed model due to the fact that the combined opening-sliding model is accompanied by a nonlinear solution. An iterative scheme is also

a good choice because it has the potential to capture a broader range of constitutive models that may be the focus of future investigation.

Unfortunately, it is not always possible *a priori* to determine whether the band is in compression or tension. This adds a non-smoothness to the equations that, in some cases, creates solution difficulties.

To this end, the slip parameter is solved using two distinct subroutines. One subroutine handles the case of positive normal traction on the band, thus solving for both opening and shear slip parameters. If the band is in compression (hence, zero normal slip on the band), a subroutine which solves solely for shear slip is utilized. If a change in the sign of the normal traction is detected within a given subroutine, then a new slip value is interpolated and used as the starting value in the appropriate subroutine. Doing this ensures that the Newton-Raphson is settling on the correct solution, given the traction state on the band.

The two subroutines differ in terms of which traction balance equations are utilized. Namely, when the band is in compression, only one equation is needed, which is the balance between the shear traction, friction and cohesive forces. In this case, the shear slip is solved for via the equation

$$\Phi = 0 = |\tau - k_s \zeta_s| - f. \tag{5.1}$$

Even if the N-R successfully yields a converged slip value, it must be ensured that the normal traction sign is negative (hence, the band is in compression) since it is possible for the band to go into a state of tension. This simply indicates that the slip on the band should instead be calculated using the combined opening-sliding formulation. In order to find the value of ζ_s at the onset of tension (hence, when $\sigma = \zeta_n = 0.0$) a simple linear interpolation is performed using Eq.5.2. We then use these new values of $\zeta_n = 0.0$ and ζ_s to initiate a N-R iteration in the opening-sliding subroutine (Eqs. 5.3 and 5.4). The three points used for interpolation are as follows: (1) (σ^i, ζ_s^i), signify the initial normal traction and slip values at the beginning of the N-R iteration, (2) $(\sigma = 0.0, \zeta_s)$, the unknown value of ζ_s when the normal traction is zero and finally (3) $\left(\sigma_f, \zeta_s^f\right)$ which are the spurious converged values of the positive normal traction and the shear slip.

$$\zeta_s \;=\; \zeta_s^i - \sigma^i \cdot \left(\frac{\zeta_s^f - \zeta_s^i}{\sigma^f - \sigma^i} \right) \tag{5.2}$$

When the band is undergoing tension, the friction force is absent, and only the normal and shear traction forces need to balanced. Thus the following set of balance equations is simultaneously solved for the normal and shear slip values:

$$\Phi_1 \;=\; 0 = \sigma - k_n \zeta_n \tag{5.3}$$
$$\Phi_2 \;=\; 0 = \tau - k_s \zeta_s \tag{5.4}$$

Again, after convergence, the normal traction sign must be checked. If it is negative (hence the band should be in compression) then the normal slip, ζ_n, will also be negative, which is of course a spurious value. In this case, a new value for ζ_s is calculated using the equation

$$\zeta_s \;=\; \zeta_s^i - \zeta_n^i \cdot \left(\frac{\zeta_s^f - \zeta_s^i}{\zeta_n^f - \zeta_n^i} \right) \tag{5.5}$$

which is the value of the shear slip at the onset of compression (i.e., when $\sigma = \zeta_n = 0.0$). After this value is found, it is used as the initial start point for the N-R iteration in the sliding-only formulation (Eq. 5.1).

The solution procedure for either formulation follows a standard Newton-Raphson approach given by

$$\zeta_{n+1}^{k+1} = \zeta_{n+1}^k - \left(\frac{\partial \Phi \left(\zeta_{n+1}^k \right)}{\partial \zeta_{n+1}^k} \right)^{-1} \Phi \left(\zeta_{n+1}^k \right) \tag{5.6}$$

5.1. *Slip Algorithm*

The solution algorithm differs in form depending on whether the element is newly localized (in which case Box 1 is used) or if slip has already begun on the band (Box 2).

Box 1: Slip algorithm for a newly localized element.

Step 1: Compute $\boldsymbol{\sigma}_{n+1}^{tr} = \boldsymbol{\sigma}_n + \boldsymbol{c}^e : \Delta\boldsymbol{\epsilon}^{conf}$

Step 2: Check for yielding on the band: $\Phi > 0$?

      If no, band is inactive. Set
          $\boldsymbol{\sigma}_{n+1} = \boldsymbol{\sigma}_{n+1}^{tr}$
          $\boldsymbol{\zeta}_{n+1} = \boldsymbol{\zeta}_n$
          and exit.

Step 3: If $\Phi > 0$, proceed to solve for slip values on the band:

      If $\sigma > 0$ (tension) solve for ζ_n and ζ_s using equations

          $\sigma - k_n\zeta_n = 0$
          $\tau - k_s\zeta_s = 0$

          After convergence, if $\sigma < 0$ then interpolate
          a new sliding value (ζ_s) using Eq.5.5 and use
          this as a starting value for the sliding-only formulation.

      Else ($\sigma < 0$, hence compression)

          Solve for ζ_s using: $|\tau - k_s\zeta_s| - f = 0$

          After convergence, if $\sigma > 0$ then interpolate
          a new sliding value using Eq.5.2 and use this
          as a starting value for the combined formulation.

Step 4: Update $\boldsymbol{\zeta}_{n+1}$, $k_{s,n+1}$, $k_{n,n+1}$ and $\boldsymbol{\sigma}_{n+1}$ then exit.

Box 2: Slip algorithm for an element which has pre-existing slip on the band.

Step 1: Compute $\boldsymbol{\sigma}_{n+1}^{tr} = \boldsymbol{\sigma}_n + \boldsymbol{c}^e : \Delta\boldsymbol{\epsilon}^{conf}$

Step 2: Check the traction on the band and enter the appropriate subroutine. First, assume elastic unloading/reloading on the band, hence hold k_s and k_n as constant and proceed to solve the balance equation(s).

    If $\sigma > 0$ (tension) solve for ζ_n and ζ_s using equations

$$\sigma - k_n\zeta_n = 0$$
$$\tau - k_s\zeta_s = 0$$

    Else ($\sigma < 0$, hence compression)

        First, check for slip on the band:

            If $|\tau - k_s\zeta_s| < f$

                No slip on the band due to friction,
                exit with trial stress.
            Else
                Solve for ζ_s using: $|\tau - k_s\zeta_s| - f = 0$

After slip value(s) calculated in elastic unloading/reloading phase, check:

If $\zeta_{eq} < \zeta_c$
        It is confirmed that the band is either
        unloading or reloading. Therefore, update
        $\boldsymbol{\sigma}_{n+1}$ and set $\boldsymbol{\zeta}_{c,n+1} = \boldsymbol{\zeta}_{c,n}$ and exit.
Else
        The band is in the softening phase.
        Recalculate the balance equation(s) allowing k_s and k_n
        to vary as in Box 1. Additionally, interpolate as needed
        if the traction sign changes.

Step 3: Update $\boldsymbol{\zeta}_{n+1}$, $k_{s,n+1}$, $k_{n,n+1}$ and $\boldsymbol{\sigma}_{n+1}$ then exit.

---

6. Stiffness Matrix Formulation

For the strong discontinuity approach, the resulting stiffness matrix from this formulation, assuming elastic unloading in the bulk material can be derived, following [13]. We begin with two sets of equations that must be solved: the standard balance of linear momentum (here taken to be quasi-static and small strain) and the traction balance on the localized deformation band.

$$\boldsymbol{r}^e = \int_{\Omega^e} \boldsymbol{B}^t : \boldsymbol{\sigma} \mathrm{d}\Omega - \int_{\Omega^e} \boldsymbol{N}^t \boldsymbol{b} \mathrm{d}\Omega - \int_{\Gamma^e} \boldsymbol{N}^t \boldsymbol{t} \mathrm{d}\Gamma = 0 \tag{6.1}$$

$$\boldsymbol{\Phi}_{n+1} = 0 \tag{6.2}$$

Taking variations on these, we arrive at

$$\delta \boldsymbol{r}^e = \boldsymbol{K}_{dd}^e \delta \boldsymbol{d}^e + \boldsymbol{K}_{d\zeta}^e \delta \boldsymbol{\zeta}^e \tag{6.3}$$

$$\delta \boldsymbol{\Phi} = \boldsymbol{K}_{\zeta d}^e \delta \boldsymbol{d}^e + \boldsymbol{K}_{\zeta\zeta}^e \delta \boldsymbol{\zeta}^e \tag{6.4}$$

where $\boldsymbol{K}_{dd}^e$ is the standard element stiffness matrix, and the others can be shown to have the following forms:

$$\boldsymbol{K}_{d\zeta}^e = -\int_{\Omega^e} \boldsymbol{B}^t : \boldsymbol{c}^e : \frac{\partial \boldsymbol{\epsilon}}{\partial \boldsymbol{\zeta}} \mathrm{d}\Omega \tag{6.5}$$

$$\boldsymbol{K}_{\zeta d}^e = \frac{\partial \boldsymbol{\Phi}}{\partial \boldsymbol{d}} = \frac{\partial \boldsymbol{\Phi}}{\partial \boldsymbol{\sigma}} : \boldsymbol{c}^e : \boldsymbol{B} \tag{6.6}$$

$$\boldsymbol{K}_{\zeta\zeta}^e = \frac{\partial \boldsymbol{\Phi}}{\partial \boldsymbol{\zeta}} \tag{6.7}$$

The tensor $\boldsymbol{B}$ is the third-order, symmetric gradient of the nodal displacement interpolation functions, commonly referred to as the strain-displacement tensor, i.e. $B_{ijk}d_k = \epsilon_{ij}$. The last equation is convenient because it is identical to the tangent stiffness used in the local N-R for determining the slip, and the same code can be reused. The other equations can be further specified

$$\frac{\partial \epsilon_{ij}}{\partial \boldsymbol{\zeta}} = \frac{1}{2} \left\{ \begin{array}{c} \frac{\partial f^h}{\partial x_i} n_j + \frac{\partial f^h}{\partial x_j} n_i \\ \frac{\partial f^h}{\partial x_i} l_j + \frac{\partial f^h}{\partial x_j} l_i \end{array} \right\} \tag{6.8}$$

where $\boldsymbol{\zeta} = \langle \zeta_n \ \zeta_s \rangle^t$.

Additionally,

$$\left(\frac{\partial \boldsymbol{\Phi}}{\partial \boldsymbol{\sigma}} \right)_{ijk} = \frac{\partial \Phi_i}{\partial \sigma_{jk}} \tag{6.9}$$

$$\frac{\partial \Phi_1}{\partial \boldsymbol{\sigma}} = \boldsymbol{n} \otimes \boldsymbol{n} \tag{6.10}$$

$$\frac{\partial \Phi_2}{\partial \boldsymbol{\sigma}} = (\boldsymbol{n} \otimes \boldsymbol{l})^s \tag{6.11}$$

The equations for the sliding-only case are as follows

$$\frac{\partial \epsilon_{ij}}{\partial \zeta_s} = \frac{1}{2} \left(\frac{\partial f^h}{\partial x_i} l_j + \frac{\partial f^h}{\partial x_j} l_i \right) \tag{6.12}$$

and

$$\frac{\partial \Phi}{\partial \boldsymbol{\sigma}} = (\boldsymbol{n} \otimes \boldsymbol{l})^s - sign(\sigma) \, \mu \, (\boldsymbol{n} \otimes \boldsymbol{n}) \tag{6.13}$$

For the quantities corresponding to $\frac{\partial \boldsymbol{\Phi}}{\partial \boldsymbol{\zeta}}$, refer to Appendix A.

The extra degrees of freedom may be condensed at the element level in the standard way, resulting in the final element stiffness matrix

$$\boldsymbol{K}^e = \boldsymbol{K}^e_{dd} - \boldsymbol{K}^e_{d\zeta} \boldsymbol{K}^{e\,-1}_{\zeta\zeta} \boldsymbol{K}^e_{\zeta d} \tag{6.14}$$

6.1. *Enhancing Simulation Robustness*

In a comparative study of several different embedded discontinuity formulations, Jirasek [20] noted that even the most optimal enhanced finite element produces a global tangent stiffness matrix which is ill-conditioned and thus difficult to invert. Later, Jirasek and Belytschko in [21] compared the enhanced finite element method with the well-known extended finite element method (XFEM). While both methods suffer from robustness issues arising from material softening, the XFEM has fewer drawbacks than the embedded discontinuity formulation. However, in the latter framework, because of the more straight-forward implementation and the fact that the added degrees of freedom within localized elements can be statically condensed at the element level, considerable effort has been made to develop methods to circumvent the aforementioned robustness issues.

Although there are several remedies outlined in the literature, affording varying levels of success, a particular method which seems to be especially promising is an implicit-explicit integration technique, Impl-Ex, devised by Oliver and co-workers [28]. This method employs an implicit internal variable calculation at the end of the time step and on the subsequent time step, during the global N-R iteration, these values are used in a semi-implicit calculation of the stresses. The benefit of this method is that for the semi-implicit calculation a positive definite stiffness matrix results which affords the simulation significant gains with regard to robustness. The conditioning of the stiffness matrix has also been shown to improve with the method [28].

Impl-Ex Integration Method

For a given localized element, the internal variables such as plastic slip magnitude are calculated implicitly at the end of the time step, after the convergent solution of the global displacements is obtained. Typically, on the subsequent step during the global N-R iteration, the stress in a localized element is calculated using, again, a fully implicit calculation. In contrast, for the Impl-Ex method, the stress is calculated semi-implicitly, which means that the previously obtained implicit values from the prior time step are used as either semi-implicit or explicit values. The general form of the semi-implicit stress, which is recognizable as the standard predictor-corrector form used in stress

return plasticity algorithms, is given in Oliver by

$$\tilde{\boldsymbol{\sigma}}_{n+1} \;\; = \;\; \boldsymbol{\sigma}_n + \boldsymbol{c}^e : \Delta\boldsymbol{\epsilon}_{n+1} - \Delta\tilde{\lambda}_{n+1}\boldsymbol{c}^e : \frac{\partial g\left(\tilde{\boldsymbol{\sigma}}_{n+1}\right)}{\partial\tilde{\boldsymbol{\sigma}}_{n+1}} \tag{6.15}$$

Using an explicit approximation of the plastic multiplier term we have

$$\tilde{\lambda}_{n+1} \;\; = \;\; \lambda_n + \frac{\Delta t_{n+1}}{\Delta t_n}\Delta\lambda_n \tag{6.16}$$

where

$$\Delta\lambda_n \;\; = \;\; \lambda_n - \lambda_{n-1}. \tag{6.17}$$

λ_n is the value of the previous time step's plastic multiplier; it is calculated implicitly after convergence of the global N-R. Similarly, λ_{n-1} is the implicit value from the nth minus one time step. Thus, in the current time step that $\Delta\lambda_n$ is being used, it is an explicit value.

Taking the derivative of the semi-implicit stress with respect to the current strain, we obtain the so-called effective algorithmic operator

$$\boldsymbol{C}_{n+1}^{\text{eff}} \;\; = \;\; \frac{\partial\tilde{\boldsymbol{\sigma}}_{n+1}}{\partial\boldsymbol{\epsilon}_{n+1}} = \left(\boldsymbol{I} + \Delta\tilde{\lambda}_{n+1}\boldsymbol{c}^e : \tilde{\boldsymbol{A}}_{n+1}\right)^{-1} : \boldsymbol{c}^e \tag{6.18}$$

$$\tilde{\boldsymbol{A}}_{n+1} = \frac{\partial^2 g\left(\tilde{\boldsymbol{\sigma}}_{n+1}\right)}{\partial\tilde{\boldsymbol{\sigma}}_{n+1} \otimes \tilde{\boldsymbol{\sigma}}_{n+1}} \tag{6.19}$$

(Refer to Appendix B for a derivation of the effective algorithmic operator.) In applying the Impl-Ex method to our particular formulation, the semi-implicit stress is calculated accordingly:

$$\tilde{\boldsymbol{\sigma}}_{n+1} = \boldsymbol{\sigma}_n + \boldsymbol{c}^e : \Delta\boldsymbol{\epsilon}_{n+1}^{\text{conf}} - \boldsymbol{c}^e : \left(\Delta\tilde{\boldsymbol{\zeta}}_{n+1} \otimes \nabla f^h\right)^s \tag{6.20}$$

where

$$\tilde{\boldsymbol{\zeta}}_{n+1} = \left[\left(\zeta_n + \frac{\Delta t_{n+1}}{\Delta t_n} \Delta \zeta_n \right) \boldsymbol{n} + \left(\zeta_s + \frac{\Delta t_{n+1}}{\Delta t_n} \Delta \zeta_s \right) \boldsymbol{l} \right]_{n+1} \tag{6.21}$$

For the effective operator calculation, we need the explicit form of the plastic potential term. If we define the direction of the slip on the deformation band as $\hat{\boldsymbol{\zeta}}$, we have for the potential

$$\frac{\partial g\left(\tilde{\boldsymbol{\sigma}}_{n+1}\right)}{\partial \tilde{\boldsymbol{\sigma}}_{n+1}} = \hat{\boldsymbol{\zeta}}_{n+1} \otimes \nabla f^h_{n+1} \tag{6.22}$$

The explicit form is not necessary however, since $\hat{\boldsymbol{\zeta}}_{n+1} \otimes \nabla f^h_{n+1}$ is calculated during the previous time step. In this case, we freeze not only the magnitude but the direction of $\hat{\boldsymbol{\zeta}}_{n+1}$. In the current time step, then, it is explicitly known and thus, $\boldsymbol{A}_{n+1} = 0$. Therefore, the jump in the displacement field is determined from the previous time step. Hence, the effective operator reduces to

$$\boldsymbol{C}^{\text{eff}}_{n+1} = \boldsymbol{I} : \boldsymbol{c}^e = \boldsymbol{c}^e \tag{6.23}$$

Hence, while there is a slight loss of accuracy in the added assumption, a simpler formulation is recovered that is linear in the case of linear elasticity. This fact tends to improve convergence rates in examples. On a concluding note, while the Impl-Ex method provides tremendous gains in terms of numerical robustness and tractability, especially for problems with complex geometries, the drawback of this method is that accuracy and unconditional stability are sacrificed due to the semi-implicit calculation on the global step. Fortunately though, the remedy lies in simply choosing a sufficiently small time step such that the error is kept within acceptable bounds. In the numerical results section we show that with a small enough step size, the Impl-Ex produces results comparable to that of the fully implicit formulation.

7. Numerical Examples

Four numerical examples are presented here as a comparison of the sliding model versus the combined sliding-opening model.

7.1. *Plane strain compression and tension of a column using a uniform load*

7.1.1. Plane strain compression test

The first example is a pressure-confined column subjected to a uniform displacement (Figure 6). The loading is quasi-static; hence, inertial effects are neglected. The bottom of the specimen is fixed so that it cannot translate vertically. In addition, one node is fixed horizontally so that the specimen is allowed to expand laterally. A confining pressure of 25 MPa is applied on both sides of the specimen. The pressure is applied at the onset of the simulation resulting in a uniform stress state throughout the mesh. This stress state causes all of the elements to localize in the same time step. This being the case, a seed element has to be chosen so that one dominant band will propagate throughout the mesh. When this initial element localizes, the band tracking algorithm will generate a single band from the seed element at the critical orientation and terminate at the opposite end of the mesh.

TABLE 1
Material parameters for plain strain compression sample

Parameter	Symbol	Value
Young's Modulus	E	5500 MPa
Poisson's Ratio	ν	0.25
Cohesive Strength Parameter	α	8.034 MPa
Friction Parameter	β	0.633
Dilation Parameter	b	0.633
Hardening Modulus	H	-10 MPa
Localized Friction Coefficient	μ	0.72
Characteristic Slip Distance	ζ^*	0.5 mm

The reaction force graph shows a characteristic elastic response as the material resists deformation, followed by a brief plastic response and then failure.
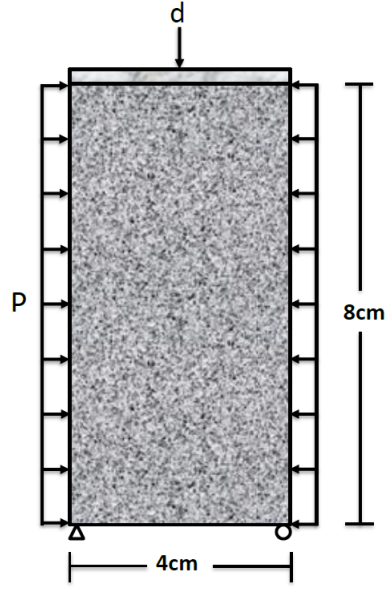
Fig 6: Geometry and loading for plane strain compression model. Simple constraints on the bottom allowing lateral expansion.

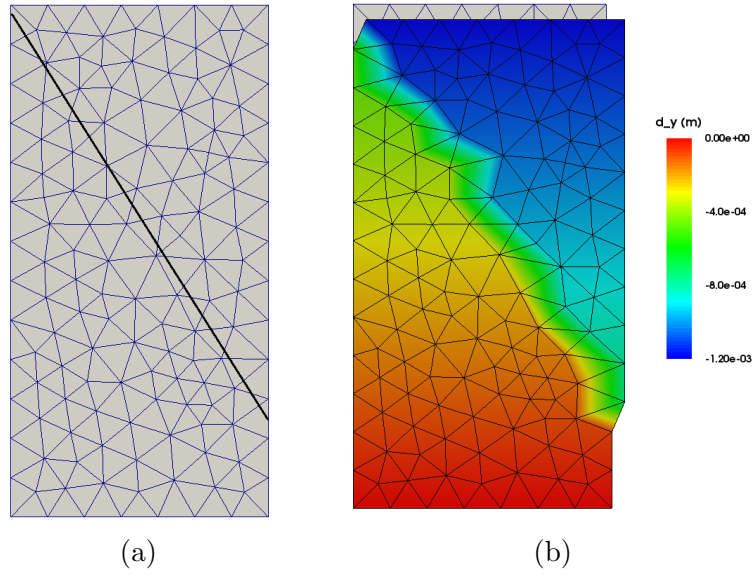(a)   (b)

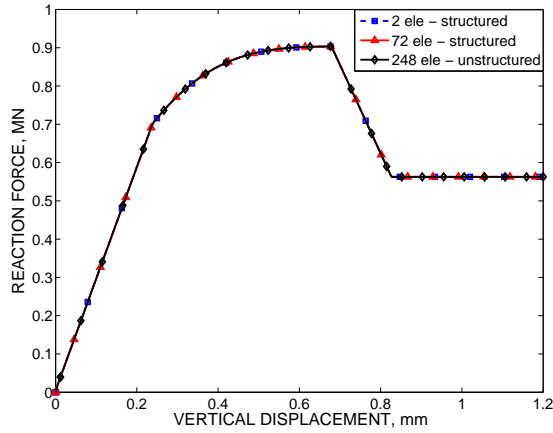Fig 7: Localization lines and deformed shape of the plane.

Fig 8: The graph shows the characteristic elastic and plastic responses as well as a stress drop and a constant frictional response.

In quasi-brittle and rock-like materials, at low confining stresses, a narrow plastic region is expected due to the low ductility. After plasticity, failure occurs in which deformation in the localized elements is concentrated solely on the slip surface while the bulk material of the element unloads elastically. After the cohesion is fully degraded a constant friction force response is observed. Both the combined and sliding-only formulations produce identical results. This is to be expected since in a purely compressive state, both formulations simplify to the sliding Mohr-Coulomb law with friction.

7.1.2. Tension test for plain-strain sample

In this example, we reverse the direction of the displacement loading from the previous example and retain the confining forces on the specimen, thus creating a uniform stress in the vertical direction. As is expected, the reversal of the displacement produces a slip line that is oriented 30°from the horizontal plane. From the reaction force profiles, the sliding-only formulation softens more quickly than the combined opening-sliding formulation due to the restricted kinematics of the system. A larger slip magnitude is required to obtain the same vertical displacement compared to the combined case, which opens in a more vertical pattern. When the cohesion degrades to

zero, both simulations fail to converge because the system becomes under-constrained (i.e., the top half of the sample has no displacement constraints in the x-direction).
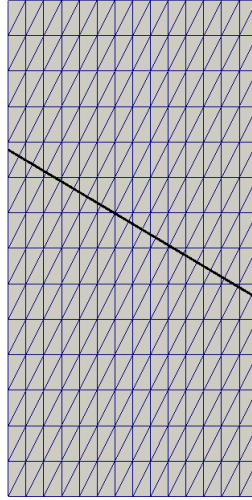
Fig 9: For the column in tension, the localization line is now oriented 30°from the horizontal plane.

7.2. *Sample with hole subjected to shearing load*

The next example, which features a slightly more complex geometrical figure, showcases the versatility that is gained from the additional opening degree of freedom. As mentioned previously, Foster et al [13] showed that the formulation involving the single degree of freedom led to spurious, mesh-dependent results. Namely, because the elements with different sliding directions are impeded by each other, stress build-up occurs around the localization zone.

For the shearing example, in the case of the sliding-only formulation, multiple bands form (13b), which produce significant locking and subsequent hardening. Notice that due to this stress build-up, neither band is able to fully propagate. Figure 14 shows a distinctive kink in the reaction force which arises due to the hardening around the localization zone. In contrast, for the combined formulation one fully formed band (13a), on each side, occurs which is concomitant with a significant stress drop in the material. For higher

(a) opening-sliding   (b) sliding-only

(c) opening-sliding   (d) sliding-only
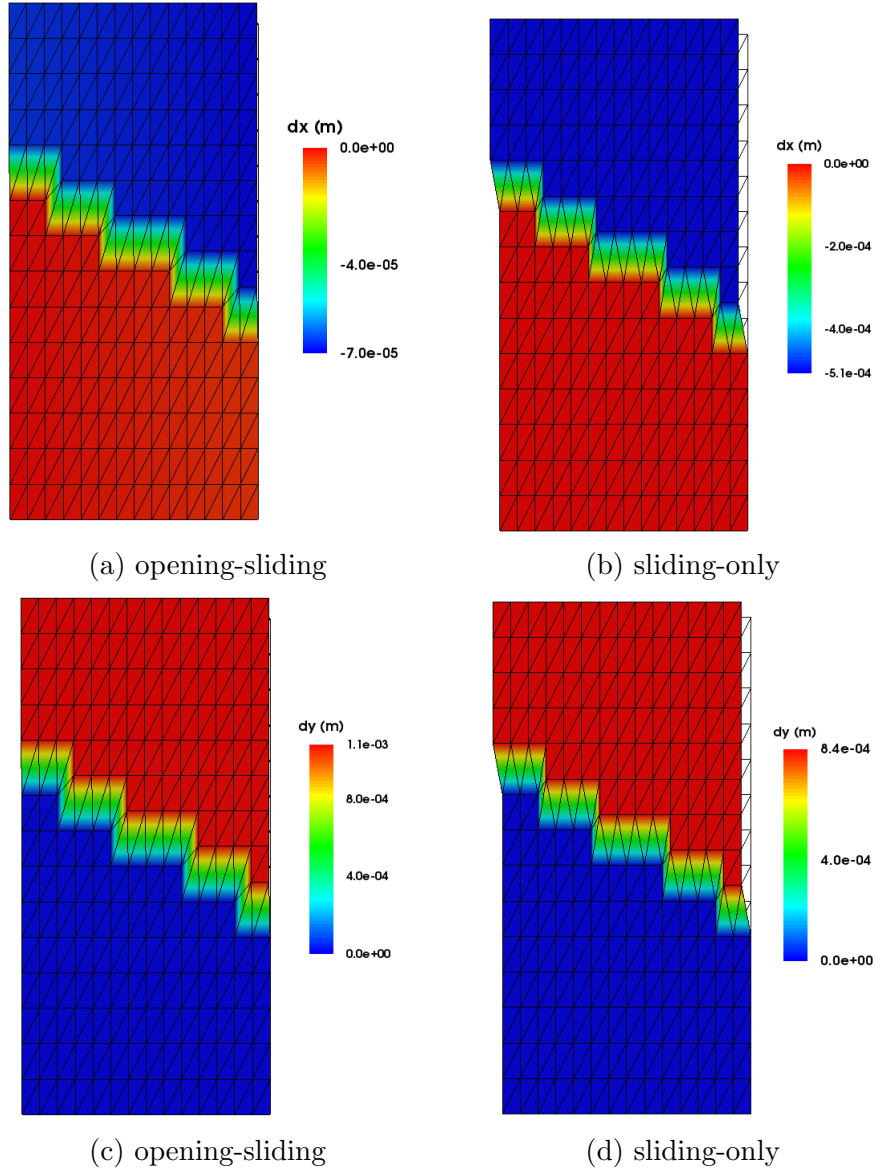
Fig 10: Comparison between the sliding-only and combined opening-sliding formulations for the pressure-confined column in tension. As expected, the sliding-only formulation shows more deformation in the horizontal direction whereas the opening-sliding model has greater deformation in the vertical direction.
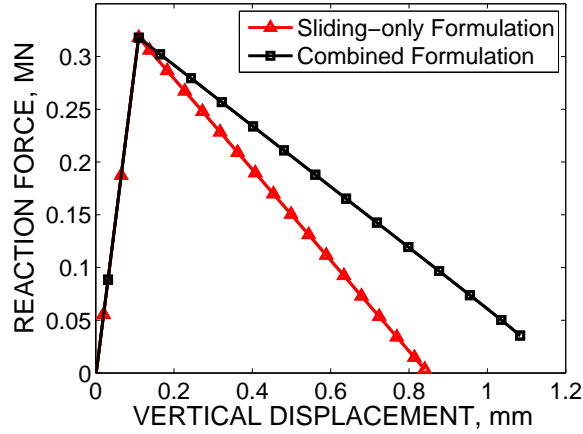
Fig 11: Both simulations fail to converge once the cohesion reaches zero. The sliding-only case softens quicker because the cohesion only acts parallel to the deformation band whereas opening-sliding formulation presents cohesion both normal and parallel to the band.

mesh refinements, after the cohesion completely degrades, there is a noticeable increase in the reaction force (16) which is due, not to geometric locking, but rather to more complex deformation patterns induced by the addition of more sampling points. This, in turn, produces an impediment to slippage, particularly at the corners where high compression is observed, resulting in the increase of shear resistance seen at the tail end of the softening curve. Nevertheless, a clear, single deformation band is observed in the deformation plot 15. Moreover, in the sliding-only formulation, the simulation is not able to complete the full loading schedule due to the interaction of multiple bands caused by the geometric locking impediment. The final case (13c) features elements which are embedded with a predefined strong discontinuity. This case was added to show that completely horizontal bands will produce a response in which the stress in the sample is completely released by the proliferation of fracture; in the absence of band curvature, the sample is allowed to freely translate in the horizontal direction.

Figure 17 shows a comparison between the Impl-Ex and fully implicit integration schemes for the shearing example with a hole, which employs only a sliding degree of freedom, comprised of 288 elements. For $\Delta t = 1.0e\text{-}2$ (a) the Impl-Ex shows noticeable oscillation, particularly at the peak and when

TABLE 2
Material parameters for sample with hole

Parameter	Symbol	Value
Young's Modulus	E	9000 MPa
Poisson's Ratio	ν	0.15
Cohesive Strength Parameter	α	8.034 MPa
Friction Parameter	β	0.633
Dilation Parameter	b	0.3165
Localized Friction Coefficient	μ	0.60
Localized Hardening Modulus	H	0.0 MPa
Characteristic Slip Distance	ζ^*	0.5 mm
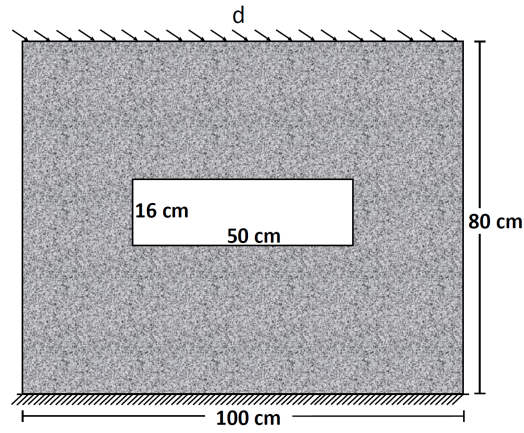
Fig 12: Boundary conditions for sample with a rectangular hole. There is a dominant shear displacement being applied to the top and a small vertical displacement which keeps the specimen from undergoing significant rotation after localization.

(a) sliding-opening

(b) sliding-only

(c) straight interface
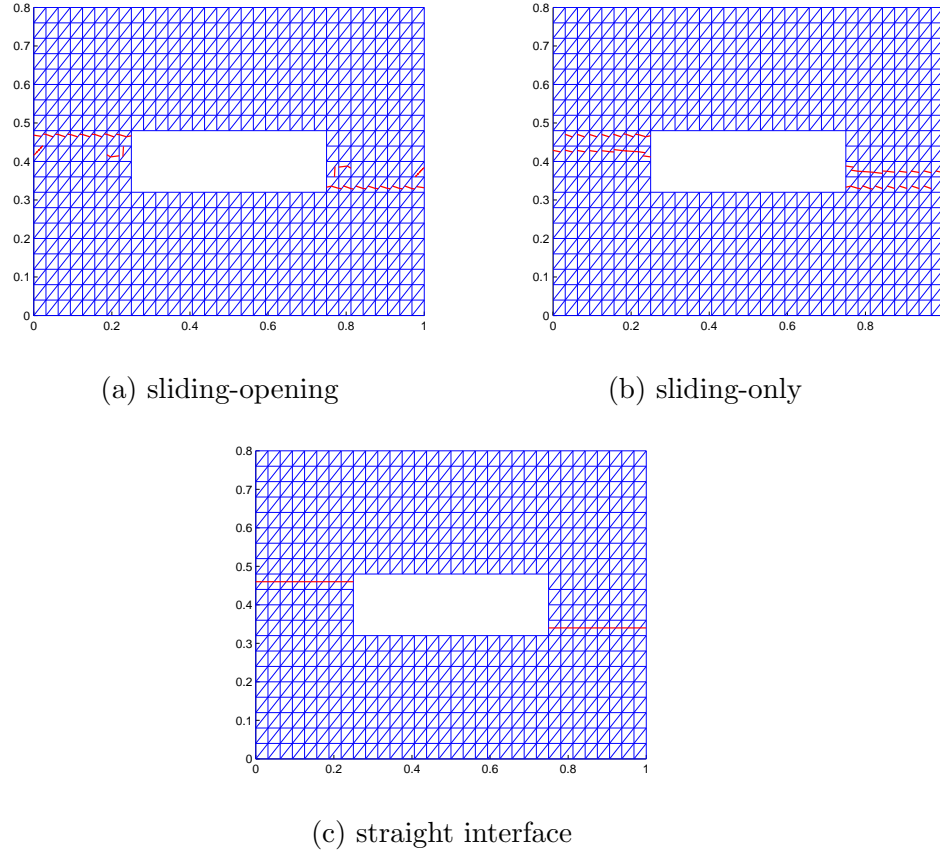
Fig 13: For the opening-sliding model (a) one dominant band is able to propagate whereas the sliding-only model (b) produces two bands both which experience locking. The bottom figure (c) displays the straight pre-embedded (interface) bands.
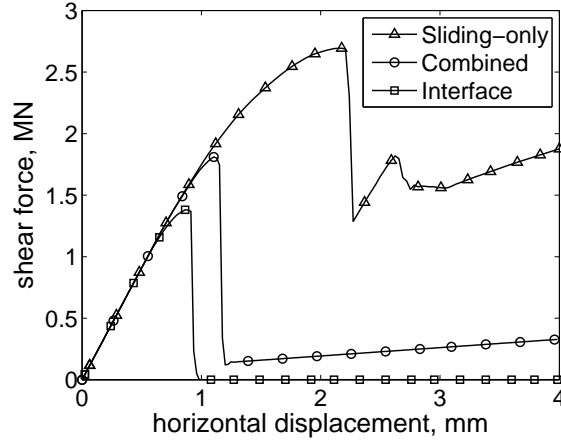
Fig 14: The sliding-only formulation shows locking which results in multiple bands, whereas the combined sliding-opening formulation shows a significant stress drop and a subsequent slight increase in stress due to some rotation of the sample at the end of the band Results are from a mesh comprised of 576 elements.

(a) sliding-only   (b) sliding-opening
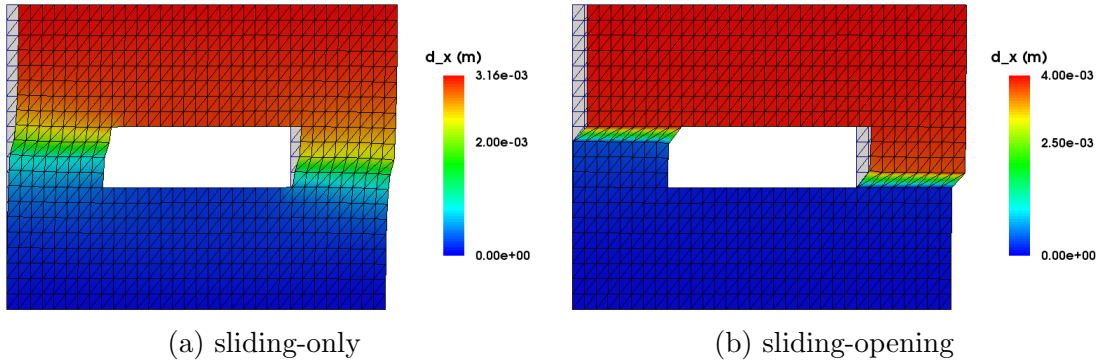
Fig 15: For the sliding-only formulation (a), two competing bands form and geometric locking ensues which produces a significant build up of bulk plasticity around the fracture zone. In the opening-sliding formulation (b), one dominant area of localization on each side of the specimen occurs, along which stress is released.
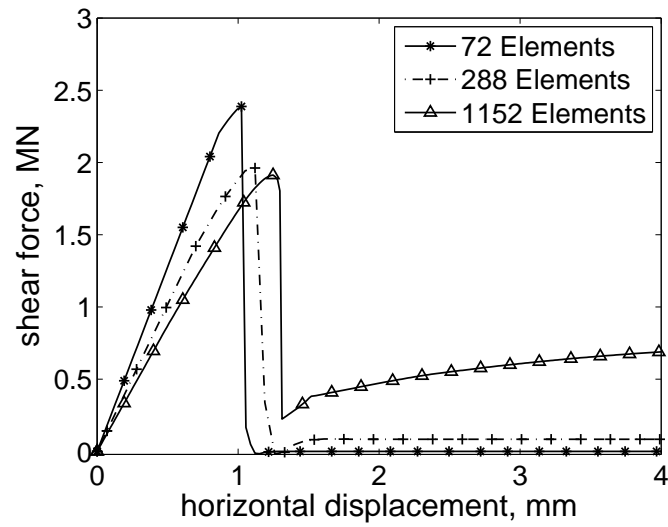
Fig 16: Convergence test for the plate with the hole run with the combined open-sliding formulation. The finest mesh shows some rise in the reaction force. This is not due to geometric locking but rather the compressive stresses at the corners of the hole.

the cohesion is significantly degraded. As the time step is refined, e.g. in the cases of Δt = 2.0e-3 (b) and Δt = 1.0e-3 (c) the Impl-Ex method is able to navigate these areas more adeptly. And in the final case of Δt = 2.0e-4 (d) the oscillation is mitigated to the point that it essentially becomes negligible. Though the time step needed for the Impl-Ex is significantly smaller than that of the fully implicit technique, it is far more robust. The fully implicit technique requires the use of elaborate time step-cutting schemes in order to reach convergence for more dense meshes, whereas the Impl-Ex does not. What is also notable is that the fully implicit is quite sensitive to the value of the critical slip parameter; if the material softens too quickly, this scheme has difficulty in capturing this quick descent and thus fails to converge at times. In contrast, because the Impl-Ex produces a positive-definite local stiffness matrix, it is not sensitive to how quickly the material softens.

7.3. *Plane strain slope stability*

This particular example is motivated by and thus similar to the one detailed in [32]. This example was chosen because it presents a very complex mix of interactions, such as high compression, tension, friction and rotation. At the top of the slope is a rigid embankment which is comprised of elements that are only allowed to undergo elastic deformation; plasticity and localized behavior are excluded. This is to prevent these elements from localizing so that softening behavior is solely relegated to the underlying material, which is the main area of interest. Figure 19 shows a comparison of the localization lines which illustrates the differing angle of descent between the two formulations. The combined formulation produces a more shallow angle. This can be understood in that the opening degree of freedom allows the material to undergo a significant amount of softening, over that of the single degree formulation, and hence less stress build-up occurs. In contrast, because geometric locking occurs in the sliding-only case, the resulting stress increase causes a steeper localization angle, more friction resistance and ultimately locking.

In addition, a significant amount of rotation is seen in the combined case because the opening degree of freedom allows the material to move much more freely than in the sliding-only case.
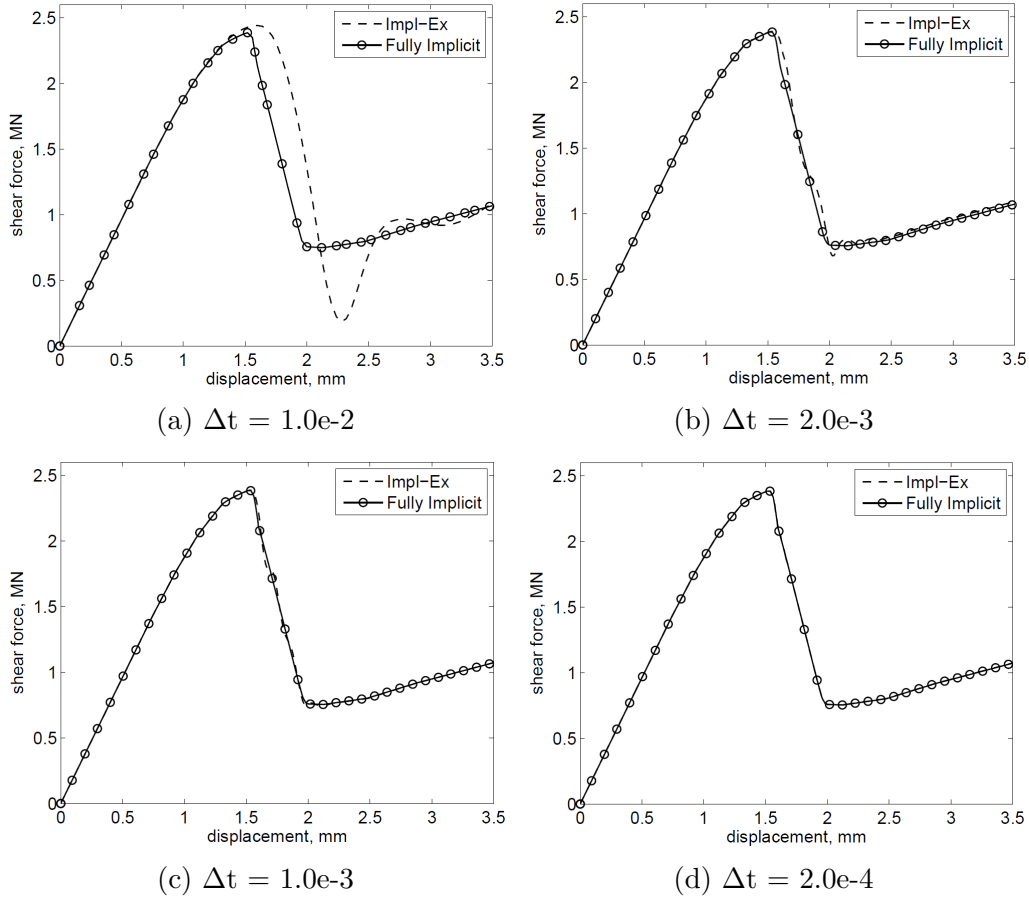
(a) $\Delta t = 1.0e\text{-}2$

(b) $\Delta t = 2.0e\text{-}3$

(c) $\Delta t = 1.0e\text{-}3$

(d) $\Delta t = 2.0e\text{-}4$

Fig 17: Comparison between the Impl-Ex and the fully implicit formulations. Sliding-only formulation with 288 elements.

TABLE 3

Material parameters for slope stability example

Parameter	Symbol	Value
Young's Modulus	E	10 MPa
Poisson's Ratio	ν	0.4
Cohesive Strength Parameter	α	40 KPa
Friction Parameter	β	0.3
Dilation Parameter	b	0.06
Localized Friction Angle	ϕ	10 °
Localized Hardening Modulus	H	0.0 MPa
Characteristic Slip Distance	ζ^*	0.4 m
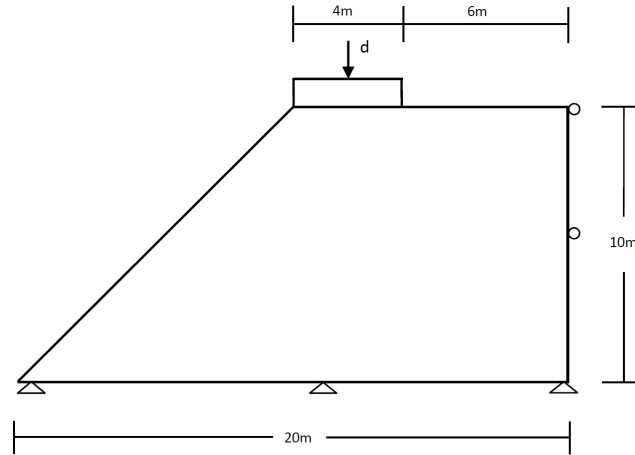
Fig 18: Slope stability problem with point load applied on embankment.
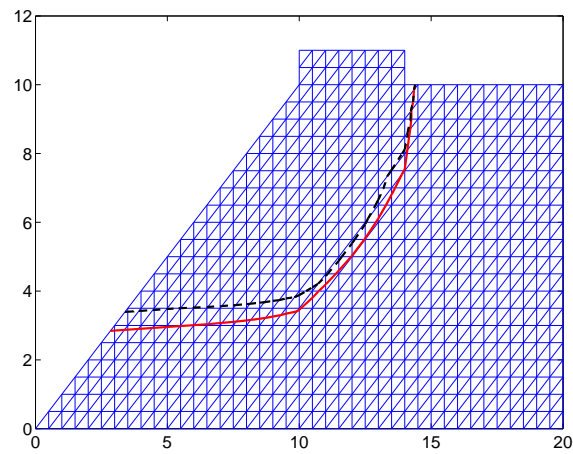
Fig 19: comparison of slip lines; the dotted black line is the opening-sliding case whereas the red line corresponds to the sliding-only case
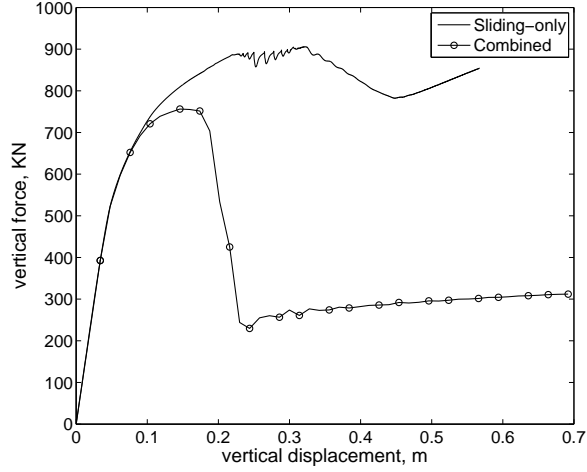
Fig 20: In the sliding-only case, there is significant friction resistance as well as locking and subsequent stress build-up. The opening-sliding formulation shows a large stress drop and resistance due to the slope rotation after complete cohesion degradation.

8. Conclusions

We have developed and implemented a constitutive model for localized softening geomaterials. The model accounts for differing fracture energies in tension and (mode II) shear, as well as friction along the interfaces. This model has been embedded in an enhanced strain finite element framework for modeling the propagation of discontinuities.

In simulating the initiation and propagation of localized deformation, the combined opening-sliding constitutive model alleviates the spurious geometric locking effect seen in the prior model which featured only a single sliding degree. Through several benchmark examples, the combined formulation displays expected softening as well as offers more accurate solutions, particularly in cases where tension is seen, even locally. Also, the formulation shows its versatility in large-scale problems as seen in the slope stability example. Lastly, implementation of the Impl-Ex technique affords the simulation code
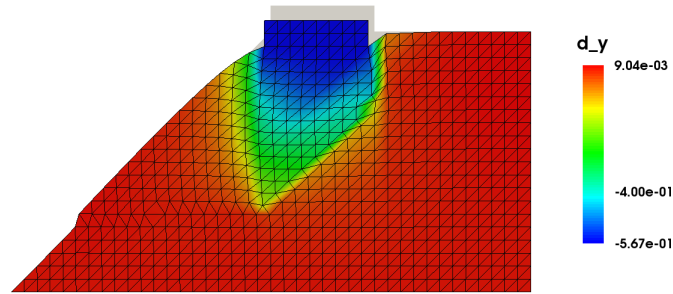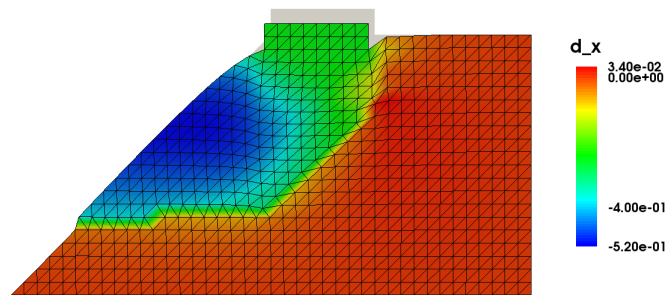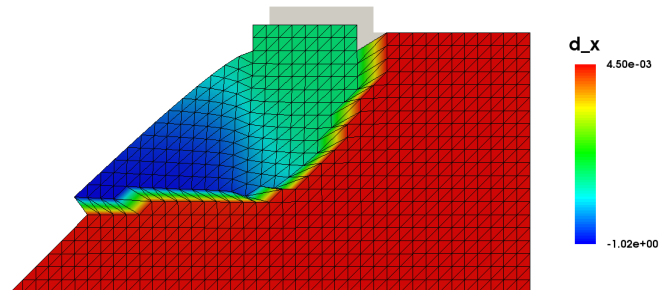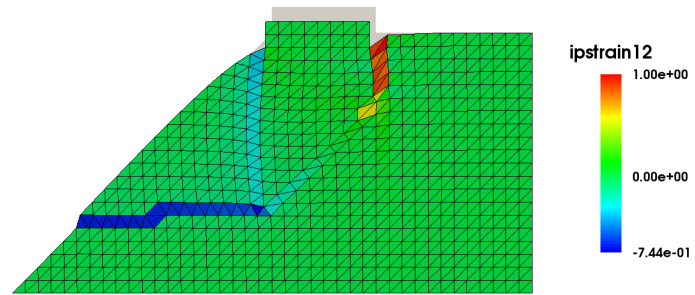
(a) sliding-only
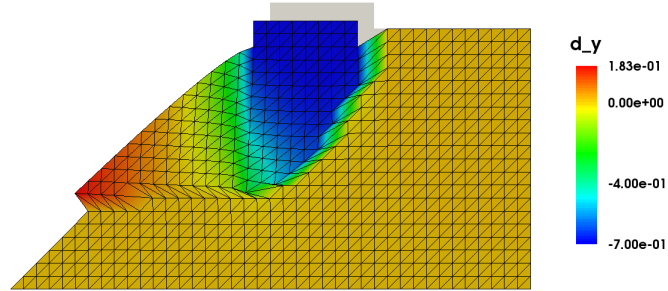
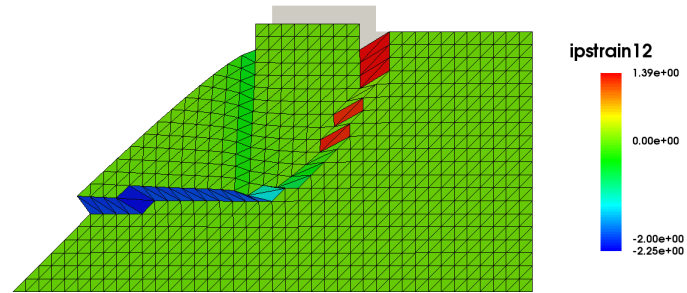(b) opening-sliding

Fig 21

(a) sliding-only

(b) opening-sliding

Fig 22

(a) sliding-only

(b) opening-sliding

Fig 23: Shear strain for a) sliding-only and b) opening-sliding cases.

significant improvements in convergence and robustness. With this in hand, the next logical step is to expand the simulations into the three-dimensional realm in order to simulate more realistic situations within a geomechanics context.

Future studies will also include the combination of the this model with a plasticity more sophisticated model suited for geomaterials, which is detailed in [14, 24]. The two models will be combined using the formulations outlined in [30]. In addition to this, the variable friction model in [13] can be incorporated so as to more accurately capture the friction behavior of geomaterials.

Acknowledgements

Appendix A: Derivatives of the Yield Functions

The gradients of the yield functions are as follows:

$$\frac{\partial \Phi_1}{\partial \zeta_n} = \frac{\partial \sigma}{\partial \zeta_n} - \left[\zeta_n \frac{\partial k_n}{\partial \zeta_n} + k_n \right] \tag{A.1}$$

$$\frac{\partial \Phi_1}{\partial \zeta_s} = \frac{\partial \sigma}{\partial \zeta_s} - \zeta_n \frac{\partial k_n}{\partial \zeta_s} \tag{A.2}$$

$$\frac{\partial \Phi_2}{\partial \zeta_n} = \frac{\partial \tau}{\partial \zeta_n} - \zeta_s \frac{\partial k_s}{\partial \zeta_n} \tag{A.3}$$

$$\frac{\partial \Phi_2}{\partial \zeta_s} = \frac{\partial \tau}{\partial \zeta_n} - \left[\zeta_s \frac{\partial k_s}{\partial \zeta_s} + k_s \right] \tag{A.4}$$

where

$$\frac{\partial k_s}{\partial \zeta_n} = \begin{cases} -\dfrac{\alpha_\zeta^2 c_0}{\zeta_c^3}\zeta_n & \text{if} \quad \zeta_{eq} = \zeta_c \\ 0 & \text{if} \quad \zeta_{eq} < \zeta_c \end{cases} \tag{A.5}$$

$$\frac{\partial k_s}{\partial \zeta_s} = \begin{cases} -\dfrac{c_0}{\zeta_c^3}\zeta_s & \text{if} \quad \zeta_{eq} = \zeta_c \\ 0 & \text{if} \quad \zeta_{eq} < \zeta_c \end{cases} \tag{A.6}$$

$$\frac{\partial k_n}{\partial \zeta_n} = \frac{\alpha_\zeta}{\alpha_\sigma}\frac{\partial k_s}{\partial \zeta_n} \tag{A.7}$$

$$\frac{\partial k_n}{\partial \zeta_s} = \frac{\alpha_\zeta}{\alpha_\sigma}\frac{\partial k_s}{\partial \zeta_s} \tag{A.8}$$

To determine the derivatives of the bulk stresses with respect to the jumps, recall

$$\boldsymbol{\sigma}_{n+1} = \boldsymbol{\sigma}_n + \boldsymbol{c}^e : \Delta\boldsymbol{\epsilon}^{\text{conf}} - \boldsymbol{c}^e : \left(\Delta\boldsymbol{\zeta} \otimes \nabla f^h\right)^s \tag{A.9}$$

Hence,

$$\frac{\partial \boldsymbol{\sigma}}{\partial \boldsymbol{\zeta}_n} = -\boldsymbol{c}^e : \left(\boldsymbol{n} \otimes \nabla f^h\right)^s \tag{A.10}$$

$$\frac{\partial \boldsymbol{\sigma}}{\partial \boldsymbol{\zeta}_s} = -\boldsymbol{c}^e : \left(\boldsymbol{l} \otimes \nabla f^h\right)^s \tag{A.11}$$

and therefore

$$\frac{\partial \sigma}{\partial \boldsymbol{\zeta}_n} = -\left(\boldsymbol{n} \otimes \boldsymbol{n}\right) : \boldsymbol{c}^e : \left(\boldsymbol{n} \otimes \nabla f^h\right)^s \tag{A.12}$$

$$\frac{\partial \sigma}{\partial \boldsymbol{\zeta}_s} = -\left(\boldsymbol{n} \otimes \boldsymbol{n}\right) : \boldsymbol{c}^e : \left(\boldsymbol{l} \otimes \nabla f^h\right)^s \tag{A.13}$$

$$\frac{\partial \tau}{\partial \boldsymbol{\zeta}_n} = -\left(\boldsymbol{n} \otimes \boldsymbol{l}\right)^s : \boldsymbol{c}^e : \left(\boldsymbol{n} \otimes \nabla f^h\right)^s \tag{A.14}$$

$$\frac{\partial \tau}{\partial \boldsymbol{\zeta}_s} = -\left(\boldsymbol{n} \otimes \boldsymbol{l}\right)^s : \boldsymbol{c}^e : \left(\boldsymbol{l} \otimes \nabla f^h\right)^s \tag{A.15}$$

Appendix B: Derivation of the Effective Algorithmic Operator

The effective algorithmic operator is defined as

$$\boldsymbol{C}_{n+1}^{\text{eff}} = \frac{\partial \tilde{\boldsymbol{\sigma}}_{n+1}}{\partial \boldsymbol{\epsilon}_{n+1}} \tag{B.1}$$

by taking the derivative of the semi-implicit stress in eq. (6.15) with respect to the implicit strain we have the following:

$$\frac{\partial \tilde{\boldsymbol{\sigma}}_{n+1}}{\partial \boldsymbol{\epsilon}_{n+1}} = \frac{\partial \boldsymbol{\sigma}_n}{\partial \boldsymbol{\epsilon}_{n+1}} + \boldsymbol{c}^e : \frac{\partial \left(\boldsymbol{\epsilon}_{n+1} - \boldsymbol{\epsilon}_n \right)}{\partial \boldsymbol{\epsilon}_{n+1}}$$
$$- \Delta \tilde{\lambda}_{n+1} \boldsymbol{c}^e : \frac{\partial}{\partial \boldsymbol{\epsilon}_{n+1}} \left(\frac{\partial g \left(\tilde{\boldsymbol{\sigma}}_{n+1} \right)}{\partial \tilde{\boldsymbol{\sigma}}_{n+1}} \right) \tag{B.2}$$

$$= \boldsymbol{c}^e : \frac{\partial \boldsymbol{\epsilon}_{n+1}}{\partial \boldsymbol{\epsilon}_{n+1}} - \Delta \tilde{\lambda}_{n+1} \boldsymbol{c}^e : \tilde{\boldsymbol{A}}_{n+1} : \frac{\partial \tilde{\boldsymbol{\sigma}}_{n+1}}{\partial \boldsymbol{\epsilon}_{n+1}}$$

where

$$\tilde{\boldsymbol{A}}_{n+1} = \frac{\partial^2 g \left(\tilde{\boldsymbol{\sigma}}_{n+1} \right)}{\partial \tilde{\boldsymbol{\sigma}}_{n+1} \otimes \tilde{\boldsymbol{\sigma}}_{n+1}} \tag{B.3}$$

Noting that $\boldsymbol{c}^e : \frac{\partial \boldsymbol{\epsilon}_{n+1}}{\partial \boldsymbol{\epsilon}_{n+1}} = \boldsymbol{c}^e : \boldsymbol{I} = \boldsymbol{c}^e$, we group terms and factor:

$$\frac{\partial \tilde{\boldsymbol{\sigma}}_{n+1}}{\partial \boldsymbol{\epsilon}_{n+1}} = \boldsymbol{c}^e - \Delta \tilde{\lambda}_{n+1} \boldsymbol{c}^e : \tilde{\boldsymbol{A}}_{n+1} : \frac{\partial \tilde{\boldsymbol{\sigma}}_{n+1}}{\partial \boldsymbol{\epsilon}_{n+1}}$$

$$\boldsymbol{c}^e = \frac{\partial \tilde{\boldsymbol{\sigma}}_{n+1}}{\partial \boldsymbol{\epsilon}_{n+1}} + \Delta \tilde{\lambda}_{n+1} \boldsymbol{c}^e : \tilde{\boldsymbol{A}}_{n+1} : \frac{\partial \tilde{\boldsymbol{\sigma}}_{n+1}}{\partial \boldsymbol{\epsilon}_{n+1}}$$

$$\boldsymbol{c}^e = \left(\boldsymbol{I} + \Delta \tilde{\lambda}_{n+1} \boldsymbol{c}^e : \tilde{\boldsymbol{A}}_{n+1} \right) : \frac{\partial \tilde{\boldsymbol{\sigma}}_{n+1}}{\partial \boldsymbol{\epsilon}_{n+1}}$$

finally

$$\frac{\partial \tilde{\boldsymbol{\sigma}}_{n+1}}{\partial \boldsymbol{\epsilon}_{n+1}} = \left(\boldsymbol{I} + \Delta \tilde{\lambda}_{n+1} \boldsymbol{c}^e : \tilde{\boldsymbol{A}}_{n+1} \right)^{-1} : \boldsymbol{c}^e = \boldsymbol{C}_{n+1}^{\text{eff}} \tag{B.4}$$

References

[1] J. Alfaiate, G.N. Wells, and L.J. Sluys. On the use of embedded discontinuity elements with crack path continuity for mode-i and mixed-mode fracture. *Engineering Fracture Mechanics*, 69(6):661 – 686, 2002.

[2] M.R. Ayatollahi and M. Sistaninia. Mode ii fracture study of rocks using brazilian disk specimens. *International Journal of Rock Mechanics and Mining Sciences*, 48(5):819 – 826, 2011.

[3] Ted Belytschko, Jacob Fish, and Bruce E. Engelmann. A finite element with embedded localization zones. *Computer Methods in Applied Mechanics and Engineering*, 70(1):59 – 89, 1988.

[4] Ronaldo I Borja. A finite element model for strain localization analysis of strongly discontinuous fields based on standard galerkin approximation. *Computer Methods in Applied Mechanics and Engineering*, 190(11):1529–1549, 2000.

[5] Ronaldo I. Borja and Craig D. Foster. Continuum mathematical modeling of slip weakening in geological systems. *Journal of Geophysical Research: Solid Earth*, 112(B4):n/a–n/a, 2007.

[6] Ronaldo I. Borja and Richard A. Regueiro. Strain localization in frictional materials exhibiting displacement jumps. *Computer Methods in Applied Mechanics and Engineering*, 190(2021):2555 – 2580, 2001.

[7] G.T. Camacho and M. Ortiz. Computational modelling of impact damage in brittle materials. *International Journal of Solids and Structures*, 33(2022):2899 – 2938, 1996.

[8] I. Carol, P. Prat, and C. López. Normal/shear cracking model: Application to discrete crack analysis. *Journal of Engineering Mechanics*, 123(8):765–773, 1997.

[9] HAW Cornelissen, DA Hordijk, and HW Reinhardt. Experimental determination of crack softening characteristics of normalweight and lightweight concrete. *Heron*, 31(2):45–56, 1986.

[10] Alireza Daneshyar and Soheil Mohammadi. Strong tangential discontinuity modeling of shear bands using the extended finite element method. *Computational Mechanics*, 52(5):1023–1038, 2013.

[11] René de Borst, Joris J.C. Remmers, and Alan Needleman. Mesh-independent discrete numerical representations of cohesive-zone models. *Engineering Fracture Mechanics*, 73(2):160 – 177, 2006. Advanced Fracture Mechanincs for Life Safety Assessments.

[12] James H. Dieterich and M. F. Linker. Fault stability under conditions of

variable normal stress. *Geophysical Research Letters*, 19(16):1691–1694, 1992.

[13] C. D. Foster, R. I. Borja, and R. A. Regueiro. Embedded strong discontinuity finite elements for fractured geomaterials with variable friction. *International Journal for Numerical Methods in Engineering*, 72(5):549–581, 2007.

[14] C.D. Foster, R.A. Regueiro, A. F. Fossum, and R. I. Borja. Implicit numerical integration of a three-invariant, isotropic/kinematic hardening cap plasticity model for geomaterials. *Computer Methods in Applied Mechanics and Engineering*, 194(50 − 52):5109 − 5138, Dec 2005.

[15] J.C. Gálvez, D.A. Cendón, and J. Planas. Influence of shear parameters on mixed-mode fracture of concrete. *International Journal of Fracture*, 118(2):163–189, 2002.

[16] GV Guinea, J Planas, and M Elices. A general bilinear fit for the softening curve of concrete. *Materials and Structures*, 27(2):99–105, 1994.

[17] R. Hill. Acceleration waves in solids. *Journal of the Mechanics and Physics of Solids*, 10(1):1 − 16, 1962.

[18] A. Hillerborg, M. Modéer, and P.-E. Petersson. Analysis of crack formation and crack growth in concrete by means of fracture mechanics and finite elements. *Cement and Concrete Research*, 6(6):773 − 781, 1976.

[19] Yoshiaki Ida. Cohesive force across the tip of a longitudinal-shear crack and griffith's specific surface energy. *Journal of Geophysical Research*, 77(20):3796–3805, 1972.

[20] Milan Jirásek. Comparative study on finite elements with embedded discontinuities. *Computer Methods in Applied Mechanics and Engineering*, 188(13):307 − 330, 2000.

[21] Milan Jirásek and Ted Belytschko. Computational resolution of strong discontinuities. In *Proceedings of Fifth World Congress on Computational Mechanics, WCCM V, Vienna University of Technology, Austria*, 2002.

[22] K. Mair and S. Abe. Breaking up: Comminution mechanisms in sheared simulated fault gouge. *Pure and Applied Geophysics*, 168(12):2277–2288, 2011.

[23] J. Mosler and G. Meschke. 3d modelling of strong discontinuities in elastoplastic solids: fixed and rotating localization formulations. *International Journal for Numerical Methods in Engineering*, 57(11):1553–1576, 2003.

[24] M.H. Motamedi and C. D. Foster. An improved implicit numerical

integration of a non-associated, three-invariant cap plasticity model with mixed isotropickinematic hardening for geomaterials. *International Journal For Numerical and Analytical Methods in Geomechanics*, 2015.

[25] J. Oliver. On the discrete constitutive models induced by strong discontinuity kinematics and continuum constitutive equations. *International Journal of Solids and Structures*, 37(4850):7207 – 7229, 2000.

[26] J. Oliver, A. E. Huespe, and E. Samaniego. A study on finite elements for capturing strong discontinuities. *International Journal for Numerical Methods in Engineering*, 56(14):2135–2161, 2003.

[27] J. Oliver and A.E. Huespe. Theoretical and computational issues in modelling material failure in strong discontinuity scenarios. *Computer Methods in Applied Mechanics and Engineering*, 193(2729):2987 – 3014, 2004. Computational Failure Mechanics for Geomaterials.

[28] J. Oliver, A.E. Huespe, S. Blanco, and D.L. Linero. Stability and robustness issues in numerical modeling of material failure with the strong discontinuity approach. *Computer Methods in Applied Mechanics and Engineering*, 195(52):7093 – 7114, 2006. Computational Modelling of Concrete.

[29] Michael Ortiz, Yves Leroy, and Alan Needleman. A finite element method for localized failure analysis. *Computer Methods in Applied Mechanics and Engineering*, 61(2):189 – 214, 1987.

[30] R. A. Regueiro and C. D. Foster. Bifurcation analysis for a rate-sensitive, non-associative, three-invariant, isotropic/kinematic hardening cap plasticity model for geomaterials: Part i. small strain. *International Journal for Numerical and Analytical Methods in Geomechanics*, 35(2):201–225, 2011.

[31] Richard A. Regueiro and Ronaldo I. Borja. A finite element model of localized deformation in frictional materials taking a strong discontinuity approach. *Finite Elements in Analysis and Design*, 33(4):283 – 315, 1999.

[32] Richard A. Regueiro and Ronaldo I. Borja. Plane strain finite element analysis of pressure sensitive plasticity with strong discontinuity. *International Journal of Solids and Structures*, 38(21):3647 – 3672, 2001.

[33] H Reinhardt. Fracture mechanics of fictitious crack propagation in concrete. *Heron*, 29(2):3–42, 1984.

[34] Alex J. Rinehart, Joseph E. Bishop, and Thomas Dewers. Fracture propagation in indiana limestone interpreted via linear softening cohesive fracture model. *Journal of Geophysical Research: Solid Earth*,

120(4):2292–2308, 2015. 2014JB011624.

[35] J.W. Rudnicki and J.R. Rice. Conditions for the localization of deformation in pressure-sensitive dilatant materials. *Journal of the Mechanics and Physics of Solids*, 23(6):371 – 394, 1975.

[36] J. C. Simo and M. S. Rifai. A class of mixed assumed strain methods and the method of incompatible modes. *International Journal for Numerical Methods in Engineering*, 29(8):1595–1638, 1990.

[37] J.C. Simo, J. Oliver, and F. Armero. An analysis of strong discontinuities induced by strain-softening in rate-independent inelastic solids. *Computational Mechanics*, 12(5):277–296, 1993.

[38] L.J. Sluys and A.H. Berends. Discontinuous failure analysis for mode-i and mode-ii localization problems. *International Journal of Solids and Structures*, 35(3132):4257 – 4274, 1998.

[39] M. Henri Tresca. On further applications of the flow of solids. *Journal of the Franklin Institute*, 106(5):326 – 334, 1878.

[40] TimothyJ. Truster and Arif Masud. A discontinuous/continuous galerkin method for modeling of interphase damage in fibrous composite systems. *Computational Mechanics*, 52(3):499–514, 2013.

[41] Yongxiang Wang and Haim Waisman. Progressive delamination analysis of composite materials using xfem and a discrete damage zone model. *Computational Mechanics*, 55(1):1–26, 2015.

[42] G.N. Wells and L.J. Sluys. Application of embedded discontinuities for softening solids. *Engineering Fracture Mechanics*, 65(23):263 – 281, 2000.

[43] T. Wu and P. Wriggers. Multiscale diffusionthermalmechanical cohesive zone model for concrete. *Computational Mechanics*, pages 1–18, 2015.

[44] Zhenjun Yang and X. Frank Xu. A heterogeneous cohesive model for quasi-brittle materials considering spatially varying random fracture properties. *Computer Methods in Applied Mechanics and Engineering*, 197(4548):4027 – 4039, 2008.

[45] Anyi Yin, Xinhua Yang, Hu Gao, and Hongping Zhu. Tensile fracture simulation of random heterogeneous asphalt mixture with cohesive crack model. *Engineering Fracture Mechanics*, 92(0):40 – 55, 2012.